

Coherent control of long-range photoinduced electron transfer by stimulated X-ray Raman processes

 Konstantin E. Dorfman^{a,1}, Yu Zhang^{b,1}, and Shaul Mukamel^{b,c,2}
^aSingapore Institute of Manufacturing Technology, Singapore 638075; ^bDepartment of Chemistry, University of California, Irvine, CA 92697; and ^cDepartment of Physics and Astronomy, University of California, Irvine, CA 92697

Contributed by Shaul Mukamel, June 30, 2016 (sent for review May 3, 2016; reviewed by Alán Aspuru-Guzik and Villy Sundstrom)

We show that X-ray pulses resonant with selected core transitions can manipulate electron transfer (ET) in molecules with ultrafast and atomic selectivity. We present possible protocols for coherently controlling ET dynamics in donor–bridge–acceptor (DBA) systems by stimulated X-ray resonant Raman processes involving various transitions between the D, B, and A sites. Simulations presented for a Ru(II)–Co(III) model complex demonstrate how the shapes, phases and amplitudes of the X-ray pulses can be optimized to create charge on demand at selected atoms, by opening up otherwise blocked ET pathways.

electron transfer | coherent control | ultrafast X-ray spectroscopy | stimulated Raman

Long-range electron transfer (ET) over tens of angstroms in molecular assemblies plays an essential role in many biological processes, artificial light-harvesting schemes, and sensor applications (1–7). Using lasers to precisely control ET pathways and rates has been a long-term goal of chemists (8). The manner in which infrared light can excite molecular vibrations to affect ET in donor–bridge–acceptor (DBA) systems has been studied theoretically (9, 10) and experimentally (11–14).

The rapid development of bright X-ray lasers and high harmonic sources has opened up new opportunities for X-ray spectroscopy (15). We have recently demonstrated that stimulated X-ray Raman spectroscopy (16, 17) with broadband X-ray pulses can reveal the time-evolving oxidation states of various species in the long-range ET process of the protein azurin (18). Here we show that by coupling to core-excited states, resonant X-ray pulses can precisely target either the donor, bridge, or the acceptor site in an ET process by altering the valence electronic states in its vicinity by triggering the bridge-to-acceptor (BA), the donor-to-bridge (DB), or the bridge-to-bridge (BB) ET transfer. We show how the ET pathways in a model DBA system ($[(\text{CN})_4\text{Ru}^{\text{II}}(\text{tpphz})\text{Co}^{\text{III}}(\text{CN})_4]^{3-}$) can be coherently manipulated by X-ray pulses resonant with the acceptor.

Application is made to a Ru–Co light-harvesting complex (shown in Fig. 1 *A* and *B*) where an electron is transferred from the donor Ru^{II} to the acceptor Co^{III} to create $\text{Ru}^{\text{III}}/\text{Co}^{\text{II}}$. X-ray pulses can create valence excitations via a Raman process (19), thus altering the occupied molecular orbitals (MOs). We shall focus on the BA ET coherent control scheme illustrated in Fig. 2*A*. In a stimulated Raman process a core hole created by the X-ray pulse on the acceptor is instantaneously filled by a valence electron on the bridge, resulting in a B→A ET. Such an ET process is analogous to the valence-to-core X-ray spontaneous emission observed in transition metal complexes with ligand-to-metal charge transfer (20).

Effective Model Hamiltonian for the Ru–Co Complex

Long-range ET in the bimetallic Ru–Co complex $[(\text{bpy})_2^1\text{Ru}^{\text{II}}(\text{tpphz})^1\text{Co}^{\text{III}}(\text{bpy})_2]^{5+}$ (low spin in the ground state) was investigated recently by transient optical absorption, X-ray absorption, X-ray diffuse scattering, and X-ray emission (21–23). This complex has been proposed for artificial light-harvesting applications. The DB ET step is very fast (<50 fs) but the BA ET is much slower (picoseconds). The system ends up in a $[(\text{bpy})_2^2\text{Ru}^{\text{III}}(\text{tpphz})^4\text{Co}^{\text{I}}(\text{bpy})_2]^{5+}$ high-spin charge-separated state. Our goal is to accelerate the BA step by a stimulated X-ray Raman process. To reduce the computational cost

while keeping the essential ET physics of the original complex, we have studied the simplified model complex $[(\text{CN})_4\text{Ru}^{\text{II}}(\text{tpphz})\text{Co}^{\text{III}}(\text{CN})_4]^{3-}$ (Fig. 1 *A* and *B*) where the bpy ligands are replaced with $(\text{CN})^-$. This eliminates the complicated spin crossover transition at the Co center (23), because the strong ligands $(\text{CN})^-$ favor the low-spin state.

The relevant ET parameters were obtained from electronic structure calculations. Because the Ru and Co centers are far apart, electronic structure calculations can be carried out for smaller fragments $[(\text{CN})_4\text{Ru}^{\text{II}}(\text{tpphz})]^{2-}$ and $[(\text{tpphz})\text{Co}^{\text{III}}(\text{CN})_4]^{2-}$ (the tpphz ligand is negatively charged). Computational details are given in *Materials and Methods*.

We model the ET in this complex using two frontier orbitals on each of the donor, the bridge, and the acceptor site; these are the highest occupied molecular orbital (HOMO) and the lowest unoccupied molecular orbital (LUMO). Neglecting spin, each site has four possible states: the ground state $|0\rangle$, where the HOMO is occupied and LUMO is not; the negatively charged state $c_m^\dagger|0\rangle$ (both orbitals are occupied); the positive charged hole state $v_m^\dagger|0\rangle$ (both orbitals are unoccupied); and a single electron–hole pair (Frenkel exciton) state $c_m^\dagger v_m^\dagger|0\rangle$, where the HOMO electron is moved to the LUMO. The operators c_m^\dagger (c_m) and v_n^\dagger (v_n) create (annihilate) an electron on site m and a hole on site n , respectively. They satisfy the Fermi commutation relations $\{c_m, c_n^\dagger\} = \delta_{mn}$, $\{v_m, v_n^\dagger\} = \delta_{mn}$. Out of all of the orbitals only three states *D*, *B*, and *A* are relevant to the ET process and are described below. Whereas the DB coupling is strong and the BA coupling is weak, we neglect the direct donor–acceptor coupling.

Initial photoexcitation creates an electron–hole pair on the donor $|D\rangle = c_d^\dagger v_d^\dagger|0\rangle$. We assume that there are no electronic coherences and only donor population is generated. This can be achieved by, e.g., resonant optical or X-ray Raman pulse that is tuned to the vicinity of the Ru atom in the donor molecule. The electron then hops from orbital *d* to orbital *b* due to the strong *D/B* coupling, thereby creating

Significance

Electron transfer is ubiquitous in chemical reactions and many biophysical processes such as respiration and photosynthesis. In this work, we show how broadband X-ray pulses can be used to change the local electronic structures of donor–bridge–acceptor (DBA) molecular systems, thus enabling and controlling electron transfer between designated sites in the molecule. An X-ray-stimulated Raman process can control electron transfer with atomic specificity and ultrafast timescale. With an appropriate X-ray pulse setting, electron pathways can be selectively enhanced. The control can be implemented at the donor, bridge, or acceptor sites in a DBA system.

Author contributions: K.E.D., Y.Z., and S.M. designed research; K.E.D. and Y.Z. performed research; K.E.D. and Y.Z. analyzed data; and K.E.D. and Y.Z. wrote the paper.

Reviewers: A.A.–G., Harvard University; and V.S., Lund University.

The authors declare no conflict of interest.

¹K.E.D. and Y.Z. contributed equally to this work.

²To whom correspondence should be addressed. Email: smukamel@uci.edu.

This article contains supporting information online at www.pnas.org/lookup/suppl/doi:10.1073/pnas.1610729113/-DCSupplemental.

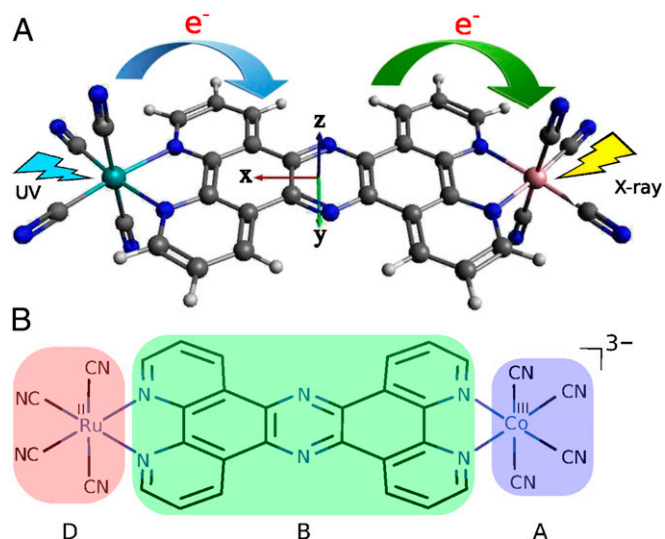


Fig. 1. (A) Three-dimensional molecular structure of the Ru-Co complex $[(\text{CN})_4\text{Ru}^{\text{II}}(\text{tpphz})\text{Co}^{\text{III}}(\text{CN})_4]^{3-}$, which is a simplified model of that studied in refs. 21–23. The D→B and B→A ET steps are represented by the blue and green arrows, respectively. The B→A ET step is aided by an X-ray pulse shot at the Co center. The coordinate axes are also shown. Color code: Ru, light blue; Co, pink; N, deep blue; C, black; H, light gray. (B) Chemical structure of the Ru-Co complex. The donor, bridge, and acceptor fragments are labeled and shaded with different colors.

state $|B\rangle = c_d c_b^\dagger |D\rangle \equiv c_b^\dagger v_d^\dagger |0\rangle$. The ET is completed when an electron hops from the bridge to acceptor due to the weak B/A coupling creating the final state: $|A\rangle = c_b c_a^\dagger |B\rangle \equiv c_a^\dagger v_d^\dagger |0\rangle$. We had calculated the matrix elements of the Hamiltonian in *SI Appendix, Eq. S1* in this diabatic basis $|D\rangle, |B\rangle, |A\rangle$.

Enabling Electron Transfer Pathways by an X-Ray Raman Process

In the absence of the X-ray pulse the ET process is described by a generalized Redfield master equation:

$$\dot{\rho} = -\mathcal{L}[\rho], \quad [1]$$

where the Liouvillian $\mathcal{L}[\rho] = i/\hbar[H_S, \rho] - K\rho$ is a rank 9 tensor in the space of D, B, A states (three populations and six coherences). Here $H_S = H_{DBA} + H_{hop}$ is a 3×3 Hamiltonian matrix which includes the DBA diagonal part H_{DBA} (*SI Appendix, Eq. S3*) plus the electron hopping off-diagonal part H_{hop} (*SI Appendix, Eq. S4*), and K denotes 9×9 Redfield ET rate matrix (*SI Appendix, Eqs. S6–S8*). The ET includes several pathways that involve both population hopping (sequential) as well as electronic coherences between adiabatic states (superexchange) (24).

The time evolution of the acceptor population can be observed by various spectroscopic measurements including fluorescence and transient absorption. Using Eq. 1 we had calculated acceptor population. After photoexcitation of the excited state population of the donor state D at time $t = 0$ in the diabatic basis, the electron wave packet goes through various states including the population and coherences between states D, B, A , and finally populates the acceptor state A at time t given by

$$P_A^{(0)}(t) = i\hbar \mathcal{G}_{AA,DD}(t), \quad [2]$$

where the zero superscript indicates that this is a reference calculation in the absence of the X-ray. $\mathcal{G}_{AA,DD}(t) = [e^{-\mathcal{L}t}]_{AA,DD}$ is the Liouville space Green's function matrix element that represents electron transfer dynamics between donor and acceptor populations and is given by *SI Appendix, Eq. S10*.

We now introduce an X-ray pulse at time t_1 after the photoexcitation. This pulse can promote an electron from the core orbital to the valence orbital of the acceptor, and the core hole is simultaneously filled by an electron from the bridge valence orbital. In this X-ray Raman process shown in Fig. 2A, the electron is transferred from orbital b to a via an inelastic process or from a to a and b to b via an elastic process. The ET can be controlled by an X-ray Raman excitation as long as the lifetime of the valence excited state created by the X-ray Raman process is comparable to or longer than the ET timescale. Interaction of the molecule with light is described by a dipole matter–field coupling in *SI Appendix, Eq. S13*. By placing a core electron on a valence orbital of the acceptor (orbital a) and filling this core hole with the valence electron from the bridge (orbital b), the pulse enables electrons to tunnel through the bridge and reach the acceptor. We had calculated the acceptor population induced by the X-ray pulse and its variation with t_2 (the time delay between the X-ray pulse arrival and observation time) and t_1 (the X-ray pulse delay relative to the initial photoexcitation). The ET dynamics consists of three steps (see the diagram in *SI Appendix, Fig. S1*). During t_1 (before the X-ray pulse) the system evolves according to the Redfield master equation (Eq. 1) and is promoted from population ρ_{DD} to some superposition of bridge and acceptor states ρ_{mn} , $m, n = A, B, D$. The second step is the evolution during the X-ray pulse. We use perturbation theory in the X-ray field–matter interaction with the diagram in *SI Appendix, Fig. S1*. In the first-order perturbation theory with respect to X-ray

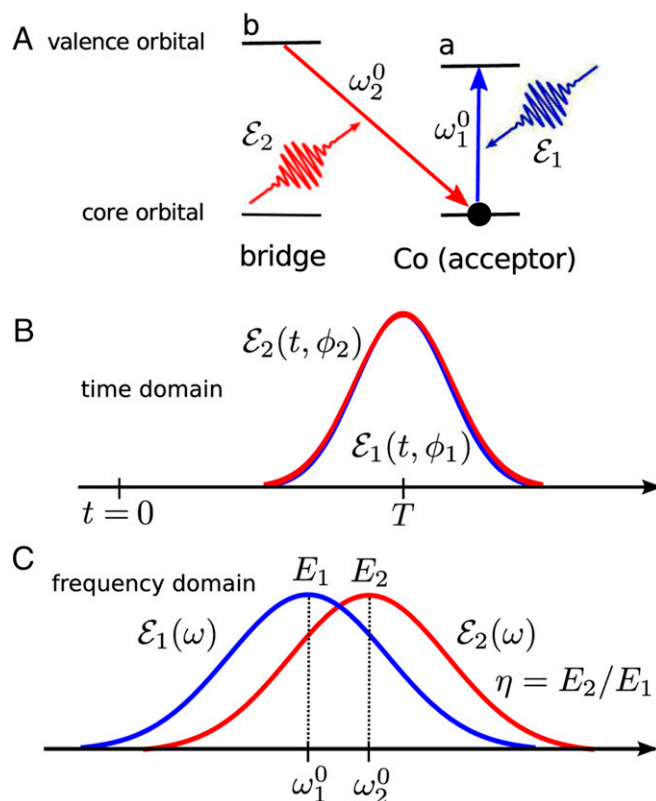


Fig. 2. (A) The acceptor control stimulated X-ray Raman process invoked by two X-ray pulses, of which the carrier frequencies ω_1^0 are resonant with the cobalt (acceptor) local core excitation and ω_2^0 is resonant with the bridge to cobalt emission transition, respectively. (B) The two pulses \mathcal{E}_1 (blue) and \mathcal{E}_2 (red) in the time domain with their phases ϕ_1 and ϕ_2 , respectively. See *SI Appendix, Eq. S14* for detailed expressions. (C) The two pulses in the frequency domain with the carrier frequencies $\omega_1^0 = 7,720.65$ eV and $\omega_2^0 = 7,721.53$ eV, bandwidths $\sigma_1 = \sigma_2 = 3$ eV, and the maximum field intensities $E_1 = E_2 = 5 \times 10^{11}$ V/cm. The amplitude ratio η is defined as E_2/E_1 . See *SI Appendix, Eq. S15* for expressions.

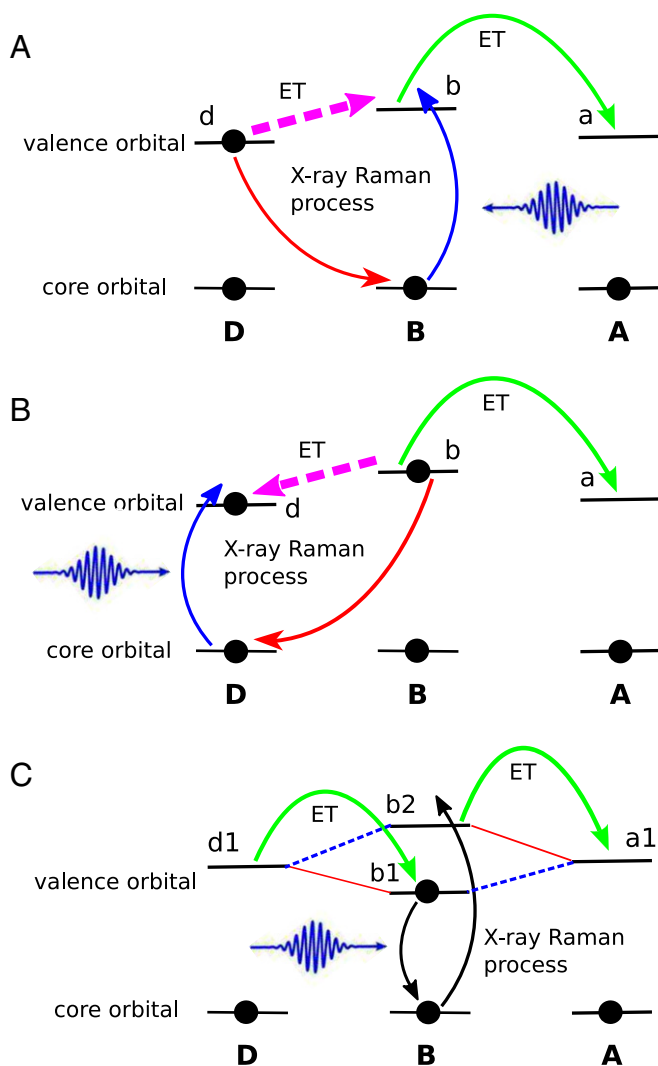


Fig. 5. The DB and BB coherent control schemes. ET processes with X-ray control are represented by magenta dashed arrows. (A) The DB control scheme which facilitates the $D \rightarrow B \rightarrow A$ ET process (core excitation on the bridge). (B) The DB control scheme which hinders the $D \rightarrow B \rightarrow A$ ET process (core excitation on the donor). (C) The BB control scheme. The red solid lines represent the strong interactions between orbitals, and blue dashed lines represent weak interactions. Relevant molecular orbitals are also labeled. Orbitals b_1 and b_2 can be on the same or different bridges.

used to coherently control the ET process in a DBA system. Alternatively, one can induce ET by an ionization with an off-resonant X-ray pulse. However, this may cause the system to decay through multiple channels, which complicates the process. Pulse delays, shapes, phases, and intensities can be tuned to enhance the ET. This coherent control tool for ET processes can be used for processing of functional electronic materials (27), disease diagnostics (28), and X-ray sterilization (29).

Infrared (IR) pulses have been used recently to excite selected vibrational modes after triggering ET by UV pulses (11, 12). In the superexchange ET mechanism, vibrations can affect the interferences between various ET pathways, so that some ET pathways could be totally switched off (9). Similar experimental observations have been reported, but for the sequential ET mechanisms (12). IR pulses only weakly perturb the electronic structure and the molecular geometry, which facilitates their application for biomolecular ET coherent control.

The X-ray pulses used here can substantially alter the electronic structure of the bridge, whereas vibrations generated by IR pulses only change phases of different ET pathways and therefore affect their interferences (9–12, 30, 31). UV-vis pulses may access the same valence excited states prepared by an X-ray Raman process. However, UV-vis excitations lack the site selectivity of X-rays. In addition, short X-ray pulses can capture ultrafast ET dynamics that goes beyond the reach of UV pulses.

Coherent control has been successfully used to manipulate the relative strength of competing optical processes (32) but the major goal has always been the steering of chemical reactions in desired directions by properly shaped and timed optical pulses (33–39). The X-ray control schemes presented here offer opportunities for manipulating and monitoring chemical reactions which involve an electron transfer step. These could provide new synthetic routes for molecules and materials. X-ray pulses allow for a molecular level control with atomic selectivity and high temporal resolution which is not possible by optical techniques (40). Our earlier studies had demonstrated that stimulated X-ray Raman spectroscopy can be used to elucidate the catalytic reaction mechanism of the cytochrome P450 complex (41) by probing the oxidation state history of reactants, products, and various intermediates. By combining narrowband and broadband pulses, the hybrid X-ray Raman technique (42) [previously denoted as attosecond stimulated X-ray Raman spectroscopy (43)] offers a unique combination of spectral and temporal resolution, making it possible to take snapshots of ultrafast chemical reaction dynamics, which is not possible by conventional IR and optical techniques. Raman lineshapes are not affected by the core lifetime and are thus much narrower than those of X-ray absorption, which significantly enhances their resolution and selectivity. Going beyond the detection of reaction intermediates, with the control schemes proposed here one can selectively enhance or suppress ET steps, thereby facilitating or hindering selected chemical reaction steps, and then probe the reacting system by additional sequences of X-ray pulses (18). These offer a class of applications to X-ray free-electron laser and high harmonic light sources.

Finally, we note that competing decay channels with the resonant X-ray Raman of a core-hole state, such as Auger electron emission, must be taken into account. Auger processes are dominant in the core-hole decay processes of light atoms, but are less important for heavy atoms. For Co, the atomic spontaneous K-edge X-ray fluorescence and Auger yields are 0.373 and 0.627, respectively (44). However, unlike the abovementioned spontaneous processes, in stimulated X-ray Raman processes intense pulses can be used to enhance the Raman cross-section and suppress the Auger decay channels. For example, it was observed that the charge-transfer excitations in NiO were enhanced by resonant X-ray Raman scattering (45). In this study we focused on the acceptor control scheme. However, we can also use the same strategy to control the electron transfer via the donor, Ru atom. For Ru, the spontaneous K-edge Auger decay yield is only 0.206 (44). Considering many heavy metal complexes used as photosensitizers in solar cell applications, it is safe to neglect the effect of Auger decay when applying our proposed X-ray electron transfer control scheme to these systems. For example, in solid-state systems, the saturation of the stimulated emission on the Si (100) surfaces with X-ray free-electron laser was observed (46), which indicates the Auger decay channels have been suppressed. It was demonstrated that the stimulated X-ray Raman in CO molecules can compete well with the Auger processes (47, 48).

Materials and Methods

The geometry of the Ru–Co model complex was optimized using the Becke three-parameter and Lee–Yang–Parr hybrid (B3LYP) exchange–correlation energy functional (49, 50). The Ru atom was described by the Stuttgart/Dresden relativistic pseudopotential and its corresponding basis set (51). The Co atom was described by the improved default triple-zeta valence basis set with small polarization (def2-TZVP) (52), and the 6–31G* basis set (53) was used for other

light atoms. Solvation effect was considered by using the polarized continuum model (54–56) with the solvent acetonitrile. Valence excited-state calculations were done at the time-dependent density functional theory (TDDFT) level of theory using the Coulomb-attenuating method version of the B3LYP functional (CAM-B3LYP) (57). All geometry optimization and valence excitation calculations were done with the quantum chemistry program package Gaussian (58). To compare the transition dipoles of charge transfer and localized core excitation around the Co center, the Co 1s core excitation calculations were done with the quantum chemistry program package NWChem (59) at the TDDFT/Tamm–Dancoff approximation (60) level of theory

using the exchange-correlation functional CAM-B3LYP. The def2-TZVP basis set was used for Co and N, and the 6–31G* basis set was used for other atoms.

ACKNOWLEDGMENTS. The support of the Chemical Sciences, Geosciences and Biosciences Division, Office of Basic Energy Sciences, Office of Science, US Department of Energy (DOE), Grant DE-FG02-04ER15571, is gratefully acknowledged. K.E.D. and Y.Z. were supported by the DOE grant. We also acknowledge the support of the National Science Foundation (Grant CHE- 1361516). K.E.D. is grateful for support from Science and Engineering Research Council at Singapore Agency for Science, Technology, and Research X-ray Photonics Program, Grant 1426500053.

- Marcus R, Sutin N (1985) Electron transfers in chemistry and biology. *Biochim Biophys Acta* 811(3):265–322.
- Marcus RA (2012) Electron transfer theory and its inception. *Phys Chem Chem Phys* 14(40):13729–13730.
- Beratan DN, et al. (2015) Charge transfer in dynamical biosystems, or the treachery of (static) images. *Acc Chem Res* 48(2):474–481.
- Winkler JR, Gray HB (2014) Long-range electron tunneling. *J Am Chem Soc* 136(8):2930–2939.
- Winkler JR, Gray HB (2014) Electron flow through metalloproteins. *Chem Rev* 114(7):3369–3380.
- Genereux JC, Barton JK (2010) Mechanisms for DNA charge transport. *Chem Rev* 110(3):1642–1662.
- Sontz PA, Muren NB, Barton JK (2012) DNA charge transport for sensing and signaling. *Acc Chem Res* 45(10):1792–1800.
- Judson RS, Rabitz H (1992) Teaching lasers to control molecules. *Phys Rev Lett* 68(10):1500–1503.
- Skourtis SS, Waldeck DH, Beratan DN (2004) Inelastic electron tunneling erases coupling-pathway interferences. *J Phys Chem B* 108(40):15511–15518.
- Antoniou P, Ma Z, Zhang P, Beratan DN, Skourtis SS (2015) Vibrational control of electron-transfer reactions: A feasibility study for the fast coherent transfer regime. *Phys Chem Chem Phys* 17(46):30854–30866.
- Lin Z, et al. (2009) Modulating unimolecular charge transfer by exciting bridge vibrations. *J Am Chem Soc* 131(50):18060–18062.
- Delor M, et al. (2014) Toward control of electron transfer in donor-acceptor molecules by bond-specific infrared excitation. *Science* 346(6216):1492–1495.
- Delor M, Sazanovich IV, Towrie M, Weinstein JA (2015) Probing and exploiting the interplay between nuclear and electronic motion in charge transfer processes. *Acc Chem Res* 48(4):1131–1139.
- Delor M, et al. (2015) On the mechanism of vibrational control of light-induced charge transfer in donor-bridge-acceptor assemblies. *Nat Chem* 7(9):689–695.
- Bucksbaum PH, Berrah N (2015) Brighter and faster: The promise and challenge of the X-ray free-electron laser. *Phys Today* 68(7):26–32.
- Mukamel S, Healion D, Zhang Y, Biggs JD (2013) Multidimensional attosecond resonant X-ray spectroscopy of molecules: lessons from the optical regime. *Annu Rev Phys Chem* 64:101–127.
- Biggs JD, Zhang Y, Healion D, Mukamel S (2012) Two-dimensional stimulated resonance Raman spectroscopy of molecules with broadband x-ray pulses. *J Chem Phys* 136(17):174117.
- Zhang Y, Biggs JD, Govind N, Mukamel S (2014) Monitoring long-range electron transfer pathways in proteins by stimulated attosecond broadband X-ray Raman spectroscopy. *J Phys Chem Lett* 5(21):3656–3661.
- Bennett K, Zhang Y, Kowalewski M, Hua W, Mukamel S (2016) Multidimensional resonant nonlinear spectroscopy with coherent broadband X-ray pulse. *Phys Scr* 2016(T169):014002.
- Pollock CJ, Delgado-Jaime MU, Atanasov M, Neese F, DeBeer S (2014) K_{β} mainline X-ray emission spectroscopy as an experimental probe of metal-ligand covalency. *J Am Chem Soc* 136(26):9453–9463.
- Torieda H, Nozaki K, Yoshimura A, Ohno T (2004) Low quantum yields of relaxed electron transfer products of moderately coupled ruthenium(II)-cobalt(III) compounds on the subpicosecond laser excitation. *J Phys Chem A* 108(22):4819–4829.
- Canton SE, et al. (2013) Toward highlighting the ultrafast electron transfer dynamics at the optically dark sites of photocatalysts. *J Phys Chem Lett* 4(11):1972–1976.
- Canton SE, et al. (2015) Visualizing the non-equilibrium dynamics of photoinduced intramolecular electron transfer with femtosecond X-ray pulses. *Nat Commun* 6:6359.
- Hu Y, Mukamel S (1989) Superexchange and electron transfer in the photosynthetic reaction center. *Chem Phys Lett* 160(4):410–416.
- Aviram A, Ratner MA (1974) Molecular rectifiers. *Chem Phys Lett* 29(2):277–283.
- Bixon M, Jortner J (1997) Electron transfer via bridges. *J Chem Phys* 107(13):5154–5170.
- Gattass RR, Mazur E (2008) Femtosecond laser micromachining in transparent materials. *Nat Photonics* 2(4):219–225.
- Dobbins JT, 3rd, Godfrey DJ (2003) Digital x-ray tomography: Current state of the art and clinical potential. *Phys Med Biol* 48(19):R65–R106.
- Fairand BP (2001) *Radiation Sterilization for Health Care Products: X-ray, Gamma, and Electron Beam* (CRC Press, Boca Raton, FL).
- Xiao D, Skourtis SS, Rubtsov IV, Beratan DN (2009) Turning charge transfer on and off in a molecular interferometer with vibronic pathways. *Nano Lett* 9(5):1818–1823.
- Carias H, Beratan DN, Skourtis SS (2011) Floquet analysis for vibronically modulated electron tunneling. *J Phys Chem B* 115(18):5510–5518.
- Silberberg Y (2009) Quantum coherent control for nonlinear spectroscopy and microscopy. *Annu Rev Phys Chem* 60:277–292.
- Levis RJ, Menkir GM, Rabitz H (2001) Selective bond dissociation and rearrangement with optimally tailored, strong-field laser pulses. *Science* 292(5517):709–713.
- Brif C, Chakrabarti R, Rabitz H (2010) Control of quantum phenomena: Past, present and future. *New J Phys* 12(7):075008.
- Moore K, Rabitz H (2012) Laser control: Manipulating molecules. *Nat Chem* 4(2):72–73.
- Tannor DJ, Rice SA (1988) *Evolution of Size Effects in Chemical Dynamics Part 1, Advances in Chemical Physics*, eds Prigogine I, Rice, SA (John Wiley & Sons, New York), Vol 70, pp 441–523.
- Engel V, Meier C, Tannor DJ (2009) *Advances in Chemical Physics*, ed Rice SA (John Wiley & Sons, New York), Vol 141, pp 29–101.
- Brixner T, Gerber G (2003) Quantum control of gas-phase and liquid-phase femtochemistry. *ChemPhysChem* 4(5):418–438.
- Nuernberger P, Wolpert D, Weiss H, Gerber G (2010) Femtosecond quantum control of molecular bond formation. *Proc Natl Acad Sci USA* 107(23):10366–10370.
- Shudo Ki, Katayama I, Ohno SY, eds (2014) *Frontiers in Optical Methods: Nano-Characterization and Coherent Control, Springer Series in Optical Sciences* (Springer, Berlin), Vol 180.
- Zhang Y, Biggs JD, Mukamel S (2015) Characterizing the intermediates compound I and II in the Cytochrome P450 catalytic cycle with nonlinear X-ray spectroscopy: A simulation study. *ChemPhysChem* 16(9):2006–2014.
- Dorfman KE, Bennett K, Mukamel S (2015) Detecting electronic coherence by multidimensional broadband stimulated X-ray Raman signals. *Phys Rev A* 92(2):023826.
- Zhang Y, Biggs JD, Hua W, Dorfman KE, Mukamel S (2014) Three-dimensional attosecond resonant stimulated X-ray Raman spectroscopy of electronic excitations in core-ionized glycine. *Phys Chem Chem Phys* 16(44):24323–24331.
- Krause MO (1979) Atomic radiative and radiationless yields for K and L shells. *J Phys Chem Ref Data* 8(2):307–327.
- Kao C, Caliebe WAL, Hastings JB, Gillet J (1996) X-ray resonant Raman scattering in NiO: Resonant enhancement of the charge-transfer excitations. *Phys Rev B Condens Matter* 54(23):16361–16364.
- Beye M, et al. (2013) Stimulated X-ray emission for materials science. *Nature* 501(7466):191–194.
- Schreck S, Beye M, Föhlich A (2015) Implications of stimulated resonant X-ray scattering for spectroscopy, imaging, and diffraction in the regime from soft to hard X-rays. *J Mod Opt* 62(Suppl 2):S34–S45.
- Kimberg V, Rohringer N (2016) Stochastic stimulated electronic x-ray Raman spectroscopy. *Struct Dyn* 3(3):034101.
- Becke AD (1993) Density-functional thermochemistry. III. The role of exact exchange. *J Chem Phys* 98(7):5648–5652.
- Stephens PJ, Devlin FJ, Chabalowski CF, Frisch MJ (1994) Ab initio calculation of vibrational absorption and circular dichroism spectra using density functional force fields. *J Phys Chem* 98(45):11623–11627.
- Andrae D, Häußermann U, Dolg M, Stoll H, Preuß H (1990) Energy-adjusted ab initio pseudopotentials for the second and third row transition elements. *Theor Chim Acta* 77(2):123–141.
- Weigend F, Ahlrichs R (2005) Balanced basis sets of split valence, triple zeta valence and quadruple zeta valence quality for H to Rn: Design and assessment of accuracy. *Phys Chem Chem Phys* 7(18):3297–3305.
- Hariharan PC, Pople JA (1973) The influence of polarization functions on molecular orbital hydrogenation energies. *Theor Chim Acta* 28(3):213–222.
- Miertuš S, Scrocco E, Tomasi J (1981) Electrostatic interaction of a solute with a continuum. A direct utilization of ab initio molecular potentials for the prevision of solvent effects. *Chem Phys* 55(1):117–129.
- Miertuš S, Tomasi J (1982) Approximate evaluations of the electrostatic free energy and internal energy changes in solution processes. *Chem Phys* 65(2):239–245.
- Pascual-ahuir JL, Silla E, Tuñon I (1994) GEPOL: An improved description of molecular surfaces. III. A new algorithm for the computation of a solvent-excluding surface. *J Comput Chem* 15(10):1127–1138.
- Yanai T, Tew DP, Handy NC (2004) A new hybrid exchange-correlation functional using the Coulomb-attenuating method (CAM-B3LYP). *Chem Phys Lett* 393(1–3):51–57.
- Frisch MJ, et al. (2009) Gaussian 09, Revision C.01 (Gaussian, Inc., Wallingford, CT).
- Valiev M, et al. (2010) NWChem: A comprehensive and scalable open-source solution for large scale molecular simulations. *Comput Phys Commun* 181(9):1477–1489.
- Hirata S, Head-Gordon M (1999) Time-dependent density functional theory within the Tamm-Dancoff approximation. *Chem Phys Lett* 314(3–4):291–299.

Supporting Information for “Coherent Control of Long-range Photoinduced Electron Transfer by Stimulated X-ray Raman Processes”

Konstantin E. Dorfman^{*}, Yu Zhang[†], and Shaul Mukamel[†]

^{*}Singapore Institute of Manufacturing Technology, 71 Nanyang Dr 638075, Singapore, and [†]Dept. of Chemistry, University of California, 450 Rowland Hall, Irvine, California 92697, USA

Submitted to Proceedings of the National Academy of Sciences of the United States of America

The Effective Hamiltonian

The system is described by the effective Hamiltonian

$$H_s = \sum_{m,n} [t_{mn}^{(e)} c_m^\dagger c_n + t_{mn}^{(h)} v_m^\dagger v_n - W_{mn}^{(eh)} c_m^\dagger v_n^\dagger v_n c_m], \quad [\text{S1}]$$

where m (n) runs over the initially unoccupied (occupied) orbitals. $t_{mn}^{(e)}$ ($t_{mn}^{(h)}$) is the electron (hole) hopping rate, $W_{mn}^{(eh)} = V_{(eh)}(|\mathbf{r}_m - \mathbf{r}_n|)$ is the Coulomb attraction between the electron and the hole. We neglect electron-electron, hole-hole Coulomb repulsion and the dipole-dipole interaction between two excitons at different sites. One can now calculate the matrix elements of the Hamiltonian in Eq. S1 in the three-state basis ($|D'\rangle, |B'\rangle, |A'\rangle$) using

$$\langle 0|c_m v_n H_s c_l^\dagger v_l^\dagger|0\rangle = \delta_{nl} t_{mk}^{(e)} + \delta_{mk} t_{nl}^{(h)} - \delta_{mk} \delta_{nl} W_{mn}^{(eh)}. \quad [\text{S2}]$$

We assume that the direct electron hopping between donor and acceptor $t_{ba}^{(e)}$ and $t_{ab}^{(e)}$ is weak compared to the donor-bridge hopping $t_{db}^{(e)}$, $t_{bd}^{(e)}$. This is justified for remote orbitals with a large energy difference - few eV. We further neglect direct hopping of electrons between donor and acceptor such that $t_{da}^{(e)} = t_{ad}^{(e)} = 0$. The Hamiltonian (Eq. S1) ($\hbar = 1$) can thus be recast as $H_s = H_{DBA} + H_{hop}$ where the diagonal part is given by

$$H_{DBA} = \omega_D |D\rangle\langle D| + \omega_B |B\rangle\langle B| + \omega_A |A\rangle\langle A|, \quad [\text{S3}]$$

and

$$H_{hop} = t_{DB} |D\rangle\langle B| + t_{BA} |B\rangle\langle A| + H.C. \quad [\text{S4}]$$

is the electron hopping Hamiltonian. Here $\omega_D = t_{d,d}^{(e)} + t_{dd}^{(h)} - W_{d,d}^{(eh)}$, $\omega_A = t_{a,a}^{(e)} + t_{dd}^{(h)} - W_{a,d}^{(eh)}$, $\omega_B = t_{b,b}^{(e)} + t_{dd}^{(h)} - W_{b,d}^{(eh)}$ are electronic energies, and $t_{DB} = t_{d,b}^{(e)}$, $t_{BA} = t_{b,a}^{(e)}$ are the hopping rates between many-electron states.

The X-ray parameters are based on the adiabatic (delocalized) basis. By diagonalizing the 3×3 Hamiltonian we obtain the adiabatic exciton Hamiltonian

$$H_s = \omega'_D |D'\rangle\langle D'| + \omega'_B |B'\rangle\langle B'| + \omega'_A |A'\rangle\langle A'|, \quad [\text{S5}]$$

where the exciton basis set is obtained via unitary transformation $U(t): \{|D', B', A'\rangle\} = U(t)\{|D, B, A\rangle\}$.

Electron Transfer Dynamics

Electron transfer dynamics in diabatic basis is described by a master equation (1) where the Liouville space components of the ET rate matrix are

$$K_{DD,DD} = k_{DB}, K_{DD,BB} = -k_{BD}, \quad [\text{S6}]$$

$$K_{BB,DD} = -k_{DB}, K_{BB,BB} = k_{BD} + k_{BA}, K_{BB,AA} = -k_{AB}, \quad [\text{S7}]$$

$$K_{AA,BB} = -k_{BA}, K_{AA,AA} = k_{AB}, \quad [\text{S8}]$$

and the rest of the components are zero. The corresponding Green's function in Liouville space is given by

$$\mathcal{G}_{mn,pq}(t) = -\frac{i}{\hbar} \theta(t) \left[e^{-\mathcal{L}t} \right]_{mn,pq}. \quad [\text{S9}]$$

Eq. (S9) can be recast as

$$\mathcal{G}_{mm,nn}(t) = -\frac{i}{\hbar} \theta(t) \sum_p \chi_{mp}^R (W_{pp})^{-1} e^{-\lambda_p t} \chi_{pn}^L. \quad [\text{S10}]$$

Here, $\chi^{L,R}$ denote the left (right) eigenvectors of the rate matrix K which satisfy the following equations

$$\sum_n \mathcal{K}_{mmnn} \chi_{np}^R = \lambda_p \chi_{mp}^R, \quad [\text{S11}]$$

and

$$\sum_m \chi_{pm}^L \mathcal{K}_{mmnn} = \lambda_p \chi_{pn}^L. \quad [\text{S12}]$$

$W = \chi^L \cdot \chi^R$ and λ_p are the identical eigenvalues for both sets of eigenvectors.

Interaction of the Molecule with X-ray Pulse

The dipole matter-field coupling is formulated in the adiabatic basis. In the interaction picture and the rotating wave approximation (RWA) (1) it reads

$$H_x'(t) = \mathbf{V}'^\dagger(t) \cdot \mathbf{E}(t-T) + \mathbf{V}'(t) \cdot \mathbf{E}^\dagger(t-T), \quad [\text{S13}]$$

where

$$\mathbf{E}(t-T) = \int_{-\infty}^{\infty} \frac{d\omega}{2\pi} \sum_{j=1,2} \mathbf{e}_j \mathcal{E}_j(\omega) e^{-i(\omega+\omega_j^0)(t-T)}, \quad [\text{S14}]$$

and

$$\mathcal{E}_j(\omega) = (2\pi)^{1/2} \sigma_j e^{-\sigma_j^2 \omega^2 / 2 - i\phi_j} \quad [\text{S15}]$$

Reserved for Publication Footnotes

is the Gaussian envelope of the component $j = 1, 2$ with pulse bandwidth σ_j and phase ϕ_j . Pulse $\mathbf{E}(t - T)$ has two components tuned such that \mathcal{E}_1 nearly resonant with $x - A'$ transition and \mathcal{E}_2 - with $x - B'$. These are the positive frequency components of the field centered at delay T , polarization unit vector \mathbf{e}_j , center frequency ω_j^0 , $j = 1, 2$. $\mathbf{V}'(t) = \sum_{n'=A',B'} \mu_{n'x} e^{-i\omega_{n'x} + \Gamma_x]t} |n'\rangle \langle x|$ represents a lowering operator that promotes an electron from core orbital x to valence orbital b' , a' . The corresponding expression in diabatic basis reads $\mathbf{V}(t) = U(t)\mathbf{V}'(t)U^{-1}(t) = \sum_{n=A,B,D} \mu_{nx} e^{-i\omega_{nx} + \Gamma_x]t} |n\rangle \langle x|$, which couples all the three diabatic states A, B, D to the core state x . The corresponding generalized polarizability tensor in diabatic basis that originates from X-ray interaction with molecule is given by Eq. (4).

Electron Transfer Control with X-ray Resonant Raman Process

The lowest order correction to acceptor population is linear in X-ray intensity. The corresponding diagram is shown in Fig. S1 (see Ref. (2) for diagram rules). One can read the diagram and obtain

$$\begin{aligned} \Delta P_A(t_1, t_2) = & 2\mathcal{R}i\hbar \int_{-\infty}^{t_1+t_2} ds_1 \int_{-\infty}^{s_1} ds_2 \sum_{i,j=1,2} \sum_{m,n,q=A,B,D} \\ & \times \mathcal{E}_i^*(s_1 - t_1) \mathcal{E}_j(s_2 - t_1) (\mathbf{e}_i \cdot \boldsymbol{\mu}_{xq}) (\mathbf{e}_j \cdot \boldsymbol{\mu}_{xm}) \\ & \times \mathcal{G}_{AA,qn}(t_1 + t_2 - s_1) \mathcal{G}_{xn,xn}(s_1 - s_2) \mathcal{G}_{mn,DD}(s_2), \end{aligned} \quad [\text{S16}]$$

where $\mathcal{G}_{xn,xn} = -i/\hbar\theta(t)e^{-(i\omega_{xn} + \Gamma_x)t}$, $n = A, B, D$ is a Liouville space greens function that governs core to valence electron dynamics. Under assumption of well separated pulses one can evaluate the time integrals in Eq. (S16) and obtain Eq. (3) in the main text. Here $i = 1$ if $q = A$, $i = 2$ if $q = B$, $j = 1$ if $m = A$ and $j = 2$ if $m = B$.

Parameters for ET Control

In the limit of well separated pulses Eq. 3 in the main text then contains dominant elastic component where $m = n = q = A$

$$\Delta P_{Ael}(t_1, t_2) = 2\mathcal{R}\mathcal{G}_{AA,AA}(t_2) |\mu_{Ax}|^2 \sigma_1^2 I_1 \mathcal{G}_{AA,DD}(t_1), \quad [\text{S17}]$$

and inelastic correction $q = n = A$, $m = B$

$$\begin{aligned} \Delta P_{Ain}(t_1, t_2) = & 2\mathcal{R}\mathcal{G}_{AA,AA}(t_2) \mathcal{G}_{BA,DD}(t_1) \\ & \times \mu_{Ax} \mu_{Bx} \sigma_1 \sigma_2 I_1^{1/2} I_2^{1/2} e^{-i\phi}. \end{aligned} \quad [\text{S18}]$$

The X-ray effect is maximal at $t_2 = 0$ and in the lowest order approximation in the weak B/A coupling we obtain

$$\frac{\Delta P_{Ain}(t_1, 0)}{\Delta P_{Ael}(t_1, 0)} \simeq \frac{\sigma_2^2 I_2^{1/2}}{\sigma_1 I_1^{1/2}} \frac{|\mu_{Bx}|}{|\mu_{Ax}|} \frac{K_{DB}}{K_{BA}} \geq 1. \quad [\text{S19}]$$

The inequality (5) in the main text therefore provides an important restriction on the pulse and matter parameters suitable for ET coherent control where the inelastic contribution originated from coherences play an important role. Under assumption of for equal parameters of the both components of the field $I_1 = I_2$, $\sigma_1 = \sigma_2$ Eq. (S19) becomes Eq. (5).

ET Parameter for the Ru-Co Model Complex

From the TDDFT excited state calculation of the Ru-Co model complex, the first valence excited state with significant Ru-to-tpphz character (D→B transition) is the No. 2 excited state with an excitation energy of 2.8013 eV. The significant MOs involved in the transition are shown in Fig. S2. To reduce the computational cost, in the B→A transition calculations, we simply use the $[\text{(-tpphz)Co}^{\text{III}}(\text{CN})_4]^{2-}$ molecular fragment cut from the Ru-Co complex. For this fragment, the first valence excited state with significant tpphz-to-Co character (B→A transition) is the No. 9 excited state with an excitation energy of 2.6070 eV. Thus we choose the following ET parameters: the donor energy 0 eV, the bridge energy $E_B = 2.8$ eV, and the acceptor energy $E_A = 2.8 + 2.6 = 5.4$ eV. The electronic couplings for the D→B and B→A ET process are estimated by using the generalized Mulliken-Hush scheme (3–6):

$$t_{DB,BA} = \frac{\mu_{12} \Delta E_{12}}{\sqrt{(\mu_1 - \mu_2)^2 + 4\mu_{12}^2}}, \quad [\text{S20}]$$

where μ_{12} is the transition dipole between the initial and final states of the ET process; ΔE_{12} is the energy difference of the initial and final states; and $\mu_{1,2}$ are the dipole moments of the initial and final state, respectively. Since the ET direction is along the x axis (see Fig. 1(a) in the main text), we consider only the x -component of the dipole in electronic coupling estimation. For t_{DB} , TDDFT calculations show $\mu_{12} = 1.6137$ a. u., $\Delta E_{12} = 2.7826$ eV, $\mu_1 = 27.0603$ Debye and $\mu_2 = 8.3054$ Debye, so $t_{DB} = 0.557512$ eV; for t_{BA} , TDDFT calculations show $\mu_{12} = 0.0362$ a. u., $\Delta E_{12} = 2.6070$ eV, $\mu_1 = -30.1568$ Debye and $\mu_2 = -60.2611$ Debye, so $t_{BA} = 0.0079674$ eV. Thus we choose $t_{DB} = 0.6$ eV and $t_{BA} = 0.008$ eV. The electron transfer times $k_{DB} = 20$ fs and $k_{BA} = 2$ ps were estimated from the experimental data in Ref. (7). Co 1s core excitation calculations on the simple Co complex fragment show that a typical Co→CN ligand core transition has a transition dipole $\mu_{Ax}^{(x)} = 0$, $\mu_{Ax}^{(y)} = -0.00003$, $\mu_{Ax}^{(z)} = -0.00086$ a. u., and a typical Co→tpphz bridge core transition has a transition dipole $\mu_{B'x}^{(x)} = 0.00033$, $\mu_{B'y}^{(y)} = 0$, $\mu_{B'z}^{(z)} = 0$ a. u., thus we used these numbers in our model simulation. Particle MOs involved in these transitions are shown in Fig. S3.

- Louisell WH (1973) Quantum Statistical Properties of Radiation (Wiley, New York).
- Mukamel S, Rahav S (2010) in Advances In Atomic, Molecular, and Optical Physics, eds Arimondo E, Berman P, Lin C (Academic Press) Vol. 59, pp 223–263.
- Cave RJ, Newton MD (1996) Generalization of the Mulliken-Hush Treatment for the Calculation of Electron Transfer Matrix Elements. Chem. Phys. Lett. 249:15–19.
- Mulliken RS (1952) Molecular Compounds and their Spectra. II. J. Am. Chem. Soc. 74:811–824.

- Hush NS (1967) in Progress in Inorganic Chemistry, ed Cotton FA (Interscience Publishers) Vol. 8, pp 391–444.
- Hush N (1968) Homogeneous and Heterogeneous Optical and Thermal Electron Transfer. Electrochim. Acta 13:1005–1023.
- Canton SE, et al. (2015) Visualizing the Non-equilibrium Dynamics of Photoinduced Intramolecular Electron Transfer with Femtosecond X-ray Pulses. Nat. Commun. 6:6359.

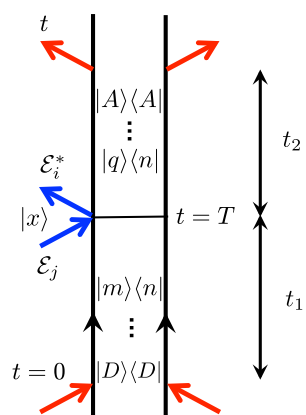


Fig. S1. Ladder diagram corresponding to $\Delta P_A(t_1, t_2)$ (Eq. (3) in the main text). Blue arrows represent interactions with X-ray pulse. Red arrows at $t = 0$ represent photo-induced ET preparation. Red arrows at t correspond to the fluorescence detection of the acceptor population. $|x\rangle$ is the intermediate resonant core state that affects the polarizability α (Eq. (4) in the main text). Diagram rules are presented in (2)

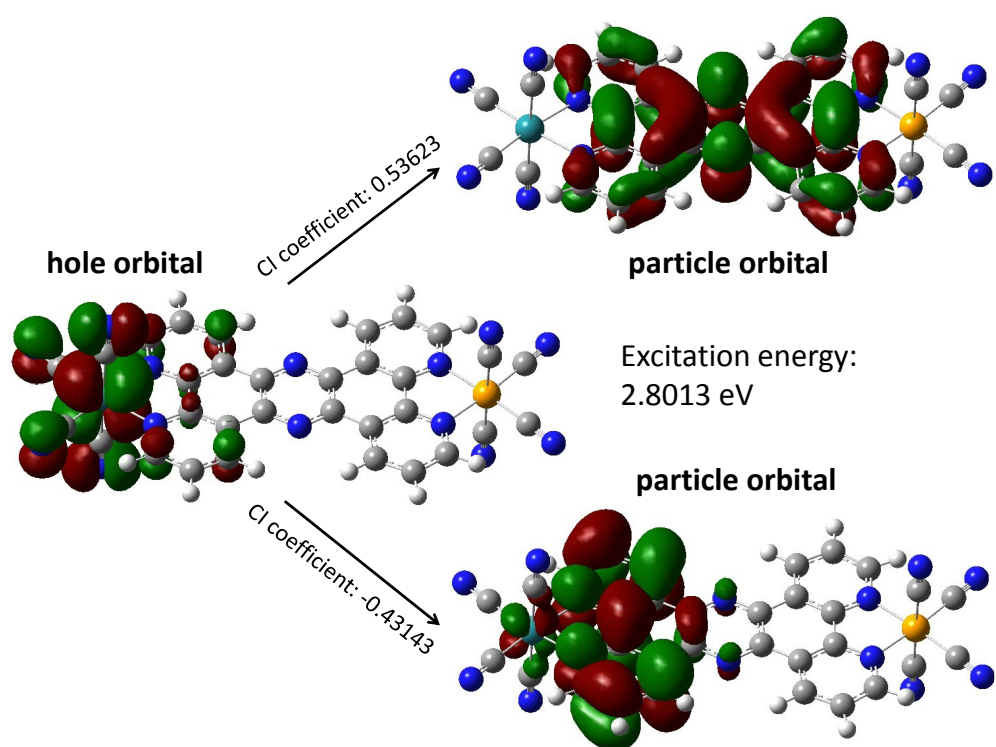


Fig. S2. Representative molecular orbitals of the D→B valence excitation of the Ru-Co model complex. The corresponding CI coefficients are also shown. Color code: Ru (light blue), Co (yellow), N (deep blue), C (gray), H (white). Results from TDDFT calculations with Gaussian09.

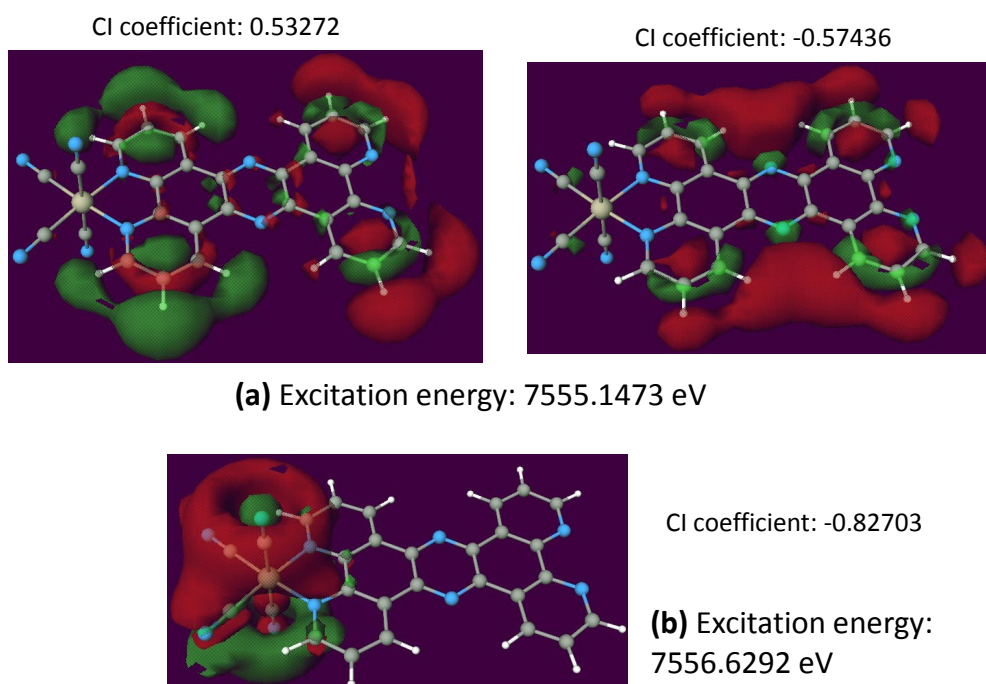


Fig. S3. Representative particle molecular orbitals of the B→A (a) and A→A local core excitation (b) of the simplified Co fragment complex. The corresponding hole orbital is always the Co 1s orbital (not shown). The corresponding CI coefficients are also shown. Color code: Co (light brown), N (blue), C (gray), H (white). Results from restricted excitation window TDDFT calculations with NWChem. Core excitation energies are not shifted.